Spatial Resolution, Measuring Time, and Fast Visualization of Hidden Deep Phantoms in Diffusion Optical Tomography of Extended Scattering Objects

V. V. Shuvalov, D. A. Chursin, and I. V. Shutov

M.V. Lomonosov Moscow State University, Vorob'evy gory, Moscow, 119899 Russia

e-mail: vsh@vsh.phys.msu.su

Received December 5, 2000

Abstract—We present the results of testing a prototype of an optical tomograph (a continuous-wave diode laser with a wavelength of 775 nm and a power of 15–20 mW) and fast algorithms for the reconstruction of the internal structure of extended (with linear sizes up to 150 mm) strongly scattering objects. Model experiments (with absorption coefficients of 0.005–0.015 and scattering coefficients of 1.4 mm^{-1}) have demonstrated that the distributions of the probability that detected photons pass through such objects (projections) can be described in terms of the coefficient of relative trajectory lengthening, whose value is independent of the arrangement of a light source and a detector. This experimental finding, confirmed by Monte Carlo numerical simulations, allows a simple scaling of projections in the case when the distance between the light source and the detector changes, thus providing an opportunity to implement fast real-time approximate statistical nonlinear algorithms for the solution of inverse and direct problems of optical tomography. Experimental testing of the prototype and the developed algorithms has shown that, for a model object with a diameter of 140 mm within the studied range of optical parameters, the coefficient of relative trajectory lengthening ranges from 1.2 to 1.9, and the reconstruction of an image of a strongly absorbing inclusion with a diameter of 1–2 mm requires no more than 0.5–1 min.

1. INTRODUCTION

Visualization of inclusions with different physical parameters in strongly scattering and weakly absorbing objects (this class of objects includes also biotissues in the near-IR range, the so-called transparency window) is an urgent problem of considerable practical importance. The early diagnosis of many diseases and injuries in medicine requires a detailed information regarding the internal structure of an affected organ. The necessity to solve this problem resulted in the development of different methods for the imaging of internal structure—tomography. All the tomographic methods are based on the presence of two substantially different characteristic spatial scales in the structure of objects being diagnosed. The problem is then to reconstruct a smooth spatial variation of certain averaged physical characteristics of an object (averaged absorption and scattering coefficients, density, electric conductivity, etc.) against small-scale (with a characteristic scale on the order of a cell size and less) changes in some physical parameters of this object (the density, chemical and molecular compositions, etc.). These smooth variations describe the averaged internal structure of an object being diagnosed. A new direction in the development of such imaging methods—optical tomography (OT) [1–3]—has appeared comparatively recently and is

rapidly growing at the moment. The main advantages of OT distinguishing this approach from other, already traditional tomographic techniques, such as X-ray [4, 5], nuclear magnetic resonance [6, 7], ultrasonic [8], and other methods of tomography, are associated with the fact that OT is virtually totally noninvasive (harmless for a patient), providing, at the same time, a spatial resolution that is acceptable in the majority of cases, allowing the costs of necessary equipment to be considerably reduced, and offering many other opportunities. The distinguishing features and the current state of art in the development and application of various tomographic techniques are summarized in Table 1. A qualitative comparison of these methods in terms of several practically important parameters is provided in Table 2.

In OT, an object being studied (diagnosed) is multiply transilluminated (along different directions) by optical radiation with known characteristics (the power of cw radiation or the energy of an input light pulse, pulse duration, the moment of time when a light pulse enters an object being diagnosed, etc.). Parameters of radiation transmitted through an object (the power of cw output radiation or the energy of an output light pulse, the waveform of the output pulse and its delay time with respect to the input pulse, etc.) are simultaneously measured. All these measurements are per-

Table 1. Specific features and the current state of art in the development of tomographic methods [45]

Influence	Measured characteristics	Application
X-ray	Attenuation constant	Diagnostics, X-ray therapy
γ radiation	Density of special markers	Functional diagnostics
Positrons	Density of special markers	Clinical testing
Magnetic field	Density of protons, relaxation time	Neurosurgery, oncology
Ultrasound	Acoustic impedance	Functional diagnostics
Electric current	Electric resistance	Clinical testing
IR radiation	Optical properties	Ophthalmology, mammography

formed either sequentially (by sequentially changing the arrangement of a radiation source and a photodetector, i.e., scanning) or in parallel (with the use of multichannel photodetectors and/or radiation sources). The above-described procedure yields a two-dimensional (2D) or four-dimensional (4D) matrix of output data, which describes the spatial distributions of intensity and/or other characteristics of output radiation for different arrangements of a radiation source and a photodetector in a discrete way in one or two independent coordinates (on the surface of an object). The total number of elements in such a matrix, N^2 or N^4, is determined by the number N of different arrangements of the light source and the photodetector. Then, one should use the matrix of output data to reconstruct the internal structure of an object, i.e., to solve the so-called inverse problem. At this stage, the mean absorption and scattering coefficients and the scattering phase function play the role of physical parameters whose spatial distributions have to be reconstructed.

Under conditions of multiple scattering (when the mean number of scattering events involving photons transmitted through an object with characteristic sizes on the order of 12–15 cm may reach 10^3 and more), it is rather difficult to solve the inverse OT problem with an adequate accuracy. The problem is that the trajectories of photons propagating through a biotissue radically differ from rectilinear trajectories, since these photons undergo multiple scattering events during the propagation process. However, the numerical solution of the so-called direct OT problem (numerical simulation of the results of real experiments, including the calculation of the output data matrix) has shown that, under conditions of the so-called small-angle scattering [9–12], some of the detected photons propagate from the source to a detector along trajectories close to rectilinear ones. These trajectories look like snakes winding around smooth curves connecting the light source and a photodetector. Such photons are usually referred to as snake photons in the literature [13]. The corresponding smooth curves form a figure reminiscent of a banana. Therefore, they are usually called banana-shape trajectories [14]. As it was shown in the late 1980s, the procedure of solving the inverse OT problem can be reduced to thoroughly developed algorithms solving inverse problems in projection X-ray tomography [15, 16], where, due to the absence of elastic scattering, the information regarding the internal structure of an object is extracted from photons propagating along a straight line. To use this approach in OT, one has to apply certain criteria to select only a small (informative) part of the total flux of detected photons that includes the photons propagating through an object along trajectories of a definite type (usually trajectories with a minimum or fixed length). Various OT techniques differ from each other by the methods of such a selection, which can be implemented in the so-called time-domain [17–19], coherence [20–23], and frequency-domain [24–27] OT. Note that the utilization of

Table 2. Comparison of different tomographic methods in terms of practically important parameters [46]: * stands for the worst parameter, while *** indicates the best parameter

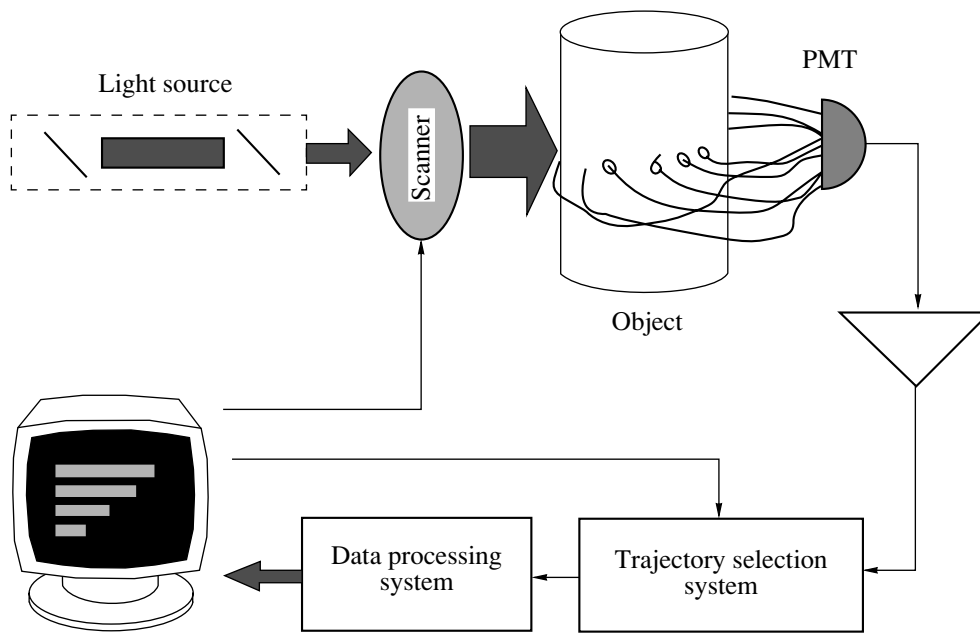| Tomographic technique	Spatial resolution, mm	Time resolution, s	Ionizing radiation	Contrast substances	Soft tissue diagnostics	Cost
X rays	3	<1	*	**	*	**
NMR	1–2	0.03	***	**	**	*
One-photon emission	7	600	*	***	**	**
Positron emission	4	600	*	***	**	**
Ultrasonic	1–2	<0.01	***	*	**	***
Electric impedance	10	0.06	***	***	***	***
Optical	0.01	<1	***	***	***	***

Fig. 1. Diagram of an optical tomograph.

only a small part of the total flux of photons transmitted through an object being diagnosed inevitably leads to a drastic lowering of the level of the informative signal and increases experimental errors. This factor relates the minimum necessary power of input laser radiation (the minimum input flux of quanta) to the maximum possible size of an object being diagnosed, the minimum time of measurements, and the limiting spatial resolution.

In spite of a tremendous number of publications on OT [1–3, 23, 28–31], there are still problems to be solved on the way toward a really efficient OT instrument. The main disadvantages of the existing devices are associated with comparatively small sizes of objects being diagnosed (one of the best results was achieved by Proskurin *et al.* [32], who increased this size up to 68 mm), a relatively slow speed of standard algorithms solving direct and inverse problems (on the order of several hours and more [28]), and many other difficulties. The purpose of this study was to develop and experimentally test a prototype of a comparatively inexpensive device capable of diagnosing strongly scattering objects with large sizes (up to 150 mm and more) and to implement fast approximate nonlinear algorithms, allowing the internal structure of such objects to be imaged virtually in real time.

2. EXPERIMENTAL

To solve the problems mentioned above, we developed a prototype of an optical tomograph based on a highly sensitive detection system with time-resolved photon counting (Fig. 1) [33]. A low-noise Hamamatsu

R636-10 photomultiplier was employed as a photodetector. Discrimination thresholds of the photon-counting system were chosen in such a way as to achieve the maximum signal-to-noise ratio. With optimal discrimination thresholds, the level of dark photocounts was 15–30 counts/s. Since such a detection system allows the amplitudes of dc and ac components of the output signal and the phase shift of the ac component to be measured, we were able to apply this system to implement the principles of frequency-domain optical tomography [27] (with a modulation frequency of 100 MHz). However, we abandoned an idea of using conventional selection methods in the experiments described below. The problem is that, when a strongly scattering object is diagnosed with radiation whose wavelength falls within the absorption band, the photons reaching the detector along longer trajectories are characterized by higher absorption probabilities and provide a lower contribution to the detected signal. Such a situation, which can be easily implemented in practice with an appropriate choice of the wavelength of probing radiation is completely equivalent to the application of one of the above-described methods of shortest trajectory selection. To the best of our knowledge, this simple approach to the selection of shortest trajectories has not been discussed in the OT literature so far. Since this method utilizes the entire flux of output radiation, it provides an opportunity not only to diagnose objects of larger sizes, but also to simplify the system by removing such elements as modulators, mode lockers, delay lines, etc., and to reduce requirements to the parameters of all the other elements of the system. Three cw diode lasers with radiation wave-

lengths of 775, 808, and 818 nm and an output power up to 300 mW can be, in principle, employed to implement this selection technique in our prototype. However, since we were able to model any optical characteristics of an object being diagnosed in our studies of model objects, all the experiments were carried out at a probing wavelength of 775 nm and a power of cw input radiation not exceeding 20 mW. Due to sufficiently strong spectral dependences of optical properties of biotissues [29, 31, 34, 35], our prototype allowed all the advantages of the so-called differential measuring systems [36] to be exploited in the case when real objects were diagnosed.

We considered an object being diagnosed as a set of uniform areas (areas where absorption coefficients μ_a, scattering coefficients μ_s, and other characteristics are constant). We assumed that all the physical parameters change in a jumpwise way only on the interfaces, and the reflection coefficients of these interfaces are negligibly small. In fact, such an assumption corresponds to a situation when optical inhomogeneities in an object are characterized by two substantially different spatial scales. Small-scale inhomogeneities are responsible for scattering processes, while the OT technique is applied to reconstruct much smoother spatial distributions of these inhomogeneities in sizes, concentrations, etc. With such an attitude, we modeled objects being diagnosed using strongly scattering media consisting of uniform mixtures of two components. One of these components (finely dispersed aqueous aliphatic emulsion) played the role of a pure scatterer ($\mu_a \cong 0$), while the second component (an aqueous solution of black ink) served as a pure absorber ($\mu_s \cong 0$). Concentration dependences of optical characteristics of both components (μ_a and the transport scattering coefficient μ_s') were determined in an experimental way. Then, mixing absorbing and scattering components in appropriate proportions, we engineered a model medium with any required optical characteristics (μ_a and μ_s') similar to the characteristics of biotissues. In the experiments described below, we have $\mu_s' \cong 1.4$ mm^{-1} and $\mu_a \cong$ 0.005–0.015 mm^{-1}, which approximately corresponds to optical characteristics of gray matter in brain [37]. The model medium was placed inside a black plastic cylindrical vessel (with a diameter of 90 or 140 mm). This vessel determined the shape of a model object being diagnosed. Vessel walls were assumed to be absolutely absorbing, which corresponded to boundary conditions employed in numerical simulations. The perimeter of the model object was divided into equal angular segments (corresponding to 30° and ~11° for the vessels with diameters of 90 and 140 mm, respectively) with special holes for input and output optical fibers (12 and 32 single-fiber plastic cables with a fiber diameter of 600 μm) located in a plane perpendicular to the symmetry axis of the vessel. Metal rods (having a shape of cylinders or parallelepipeds), whose charac-
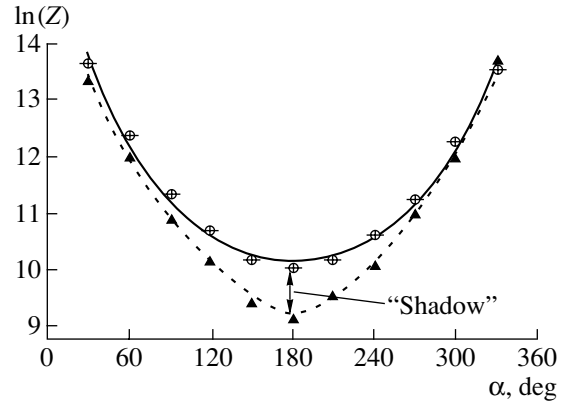

Fig. 2. Dependence of the number of photocounts Z on the position of the photodetector (the angle α) for an object with $\mu_a = 0.01$ mm^{-1}, $\mu_s' = 1.4$ mm^{-1}, and $2R = 90$ mm in the case of a strongly absorbing inclusion with $r = 7.5$ mm. Input radiation is coupled in through a fiber in position $0°$.

teristic sizes (diameters or the sizes of cross sections) were varied within the range from 4 to 25 mm served as strongly absorbing inclusions, imitating, for example, hematomas. The side surfaces of these rods were blackened.

Figure 2 illustrates the result of a typical experiment on imaging an absolutely absorbing inclusion (a black metal cylinder with a radius of 7.5 mm) placed inside an object being diagnosed. The lower curve in Fig. 2 corresponds to the case when an inclusion was placed inside an object along with absorbing and scattering components. The upper curve was obtained with no inclusion inside the object. The experimental results clearly reveal the shadow area, where the number of photons detected in the absence of an inclusion is much larger than the number of photons detected in the presence of an inclusion (for certain positions of the detector).

3. SCALING OF THE DISTRIBUTIONS

The results of our experiments (see Fig. 2) allow us to make a very important conclusion, which determines the possibility of implementing fast algorithms for the solution of both direct and inverse OT problems. All the experimental dependences obtained by probing large-size strongly scattering objects without inclusions can be satisfactorily approximated with the following function:

$$Z(L_k) \propto P/L_k^2 \exp(-\mu_a \xi L_k),$$
$$\text{where} \quad \xi = \xi(\mu_a, \mu_s').$$

(1)

Here, P is the power of input radiation, $Z(L_k)$ is the dependence of the number of photocounts on the distance $L_k = 2r\sin(\alpha_{i,k}/2)$ between the light source and the photodetector along a straight line, r is the radius of
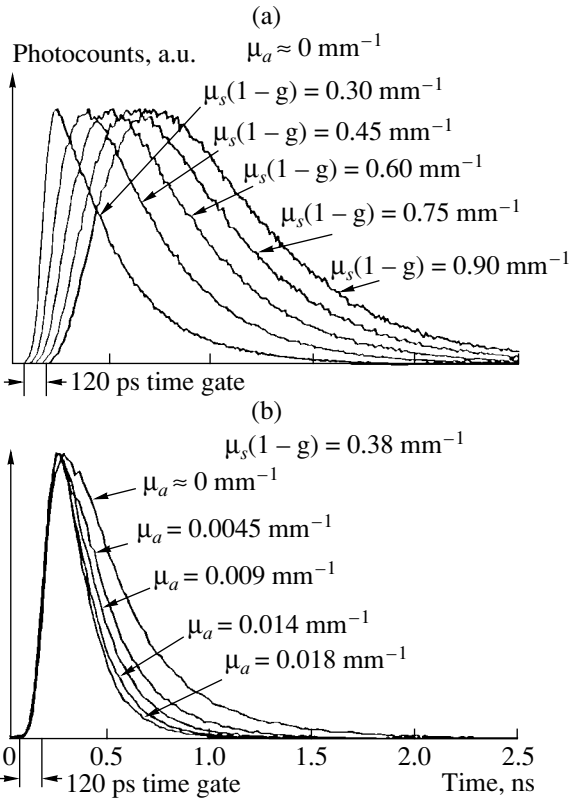
(a)

Photocounts, a.u. $\mu_a \approx 0$ mm^{-1}

$\mu_s(1 - g) = 0.30$ mm^{-1}

$\mu_s(1 - g) = 0.45$ mm^{-1}

$\mu_s(1 - g) = 0.60$ mm^{-1}

$\mu_s(1 - g) = 0.75$ mm^{-1}

$\mu_s(1 - g) = 0.90$ mm^{-1}

120 ps time gate

(b)

$\mu_s(1 - g) = 0.38$ mm^{-1}

$\mu_a \approx 0$ mm^{-1}

$\mu_a = 0.0045$ mm^{-1}

$\mu_a = 0.009$ mm^{-1}

$\mu_a = 0.014$ mm^{-1}

$\mu_a = 0.018$ mm^{-1}

0   0.5   1.0   1.5   2.0   2.5

120 ps time gate   Time, ns

Fig. 3. Dependences of time-of-flight distributions on (a) the scattering coefficient μ_s' and (b) the absorption coefficient μ_a.

Aspect ratio, ξ

2.0

1.6

1.2

■ Data
— Fitting

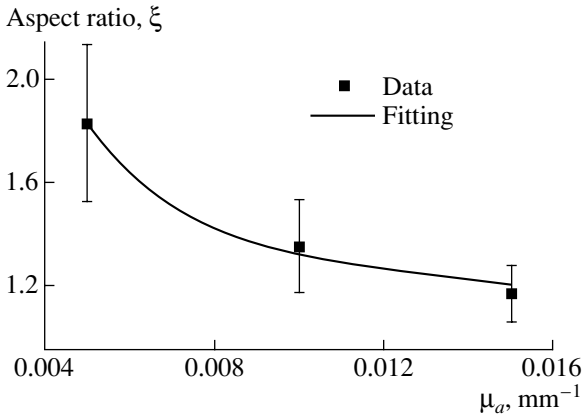0.004   0.008   0.012   0.016

μ_a, mm^{-1}

Fig. 4. The coefficient ξ of trajectory lengthening as a function of the absorption coefficient μ_a.

the vessel, $\alpha_{i,k}$ is the central angle between the positions of the light source i and the photodetector k, and ξ is the parameter determining the mean relative lengthening of the trajectories of detected photons relative to L_k. Although Eq. (1) looks very simple, it is not trivial at all. The first factor $(1/L_k^2)$ on the right-hand side of Eq. (1) describes the lowering in the intensity of output radiation due to the angular divergence of this

radiation related to scattering. The second factor explicitly depends on μ_a and involves μ_s' and μ_a through ξ. Our experiments have demonstrated that Eq. (1) perfectly (within the limits of experimental errors equal to 0.5–1.0%) describes the results of all the experiments performed in the absence of inclusions. The value of ξ is also fixed for any specific experiment (the values of μ_s' and μ_a are fixed). One of the examples of such an approximation is shown by the solid line in Fig. 2. Numerical simulations (performed with the use of the Monte Carlo method) have confirmed this fact with a much higher accuracy (better than 0.1%).

In principle, as it was recognized earlier, both the distribution of trajectories of detected photons in lengths in strongly scattering media and the most probable length of these trajectories change in response to variations in optical characteristics of the scattering medium. Figure 3 presents, for example, the results of [31] for the variation in the temporal profile of the output light pulse in time-domain OT. As can be seen from Fig. 3a, the maximum of the time-of-flight distribution is shifted to the left (which corresponds to a decrease in the most probable trajectory length) with the decrease in μ_s'. At the same time, as μ_a increases (Fig. 3b), the distribution function becomes sharper (the scatter of trajectories in lengths decreases). Therefore, it is not surprising that, when μ_a was varied within the range of 0.005–0.015 mm^{-1} in our experiments, the quantity also changed, running from 1.2 up to 1.9 (Fig. 4). The main conclusion that follows from the fact that ξ is constant is that, in the absence of inclusions, the distribution functions of the flux of detected photons in an object being diagnosed are always geometrically similar to each other, and they can be easily recalculated (scaled) through each other when the distance between the light source and the detector is changed. The latter circumstance allows the algorithm for the solution of the inverse problem described below to be implemented in real time.

4. NUMERICAL SIMULATION

The implementation of our algorithm for the approximate solution of the inverse OT problem requires certain reference data (see the discussion below), which can be obtained only by solving the relevant direct problem. In the regime of multiple scattering, the direct problem can be described in terms of the diffusion equation [38, 39], transfer matrices [40, 41], or the Monte Carlo method [14, 42]. We chose the Monte Carlo method, since this approach is more universal and can be also employed for spatial scales comparable with the mean free path length. In addition, since the required reference data are of statistical character, the use of the Monte Carlo method seems to be natural and reasonable. A few disadvantages of this technique are associated with the fact that this method
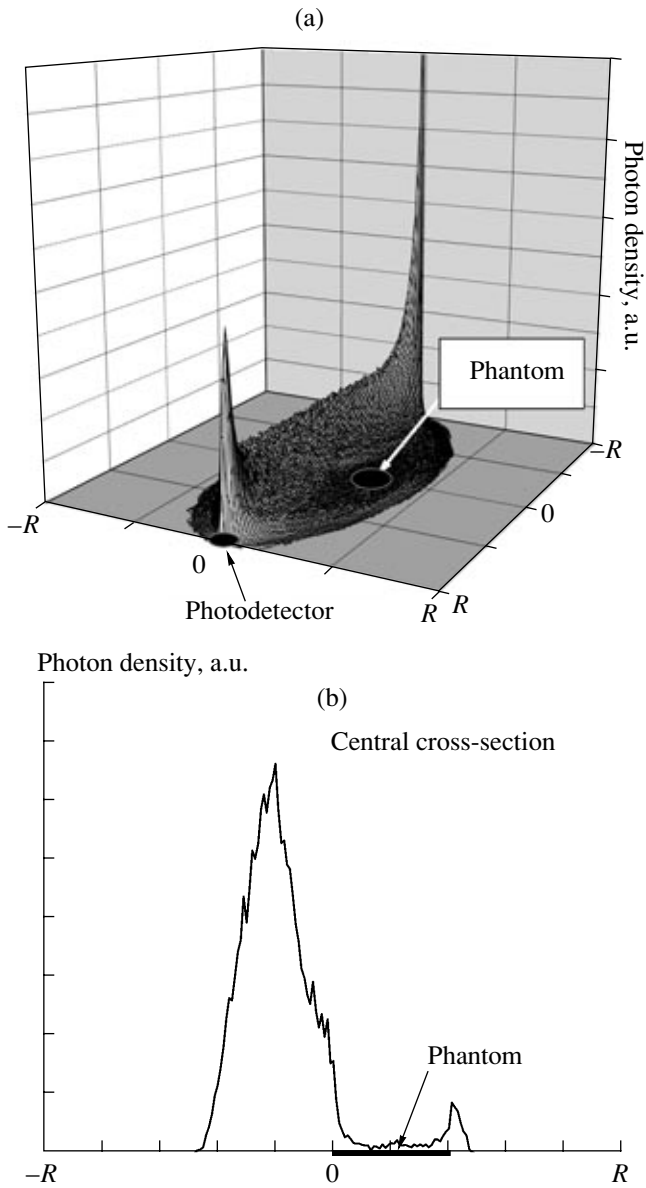
(a)

Photon density, a.u.

Phantom

−R

0

−R

0

Photodetector

R R

(a)

Photon density, a.u.

Source

−R

0

R

0

Photodetector

R −R

Photon density, a.u.

(b)

Central cross-section

Phantom

−R 0 R

Fig. 5. Cutting of photons from distributions: (a) the spatial distribution and (b) its central cross section. The object has the following parameters: $\mu_a = 0.02$ mm^{-1}, $\mu_s' = 1$ mm^{-1}, $g = 0.95$, and $2R = 10$ mm. Parameters of the inclusion are $\mu_a = 2$ mm^{-1}, $\mu_s' = 1.4$ mm^{-1}, $g = 0.95$, and $r = 1$ mm.

Photon density, a.u.

(b)

1

0

−R 0 R

Fig. 6. The spatial distribution of the probability that photons pass through (a) different points of an object and (b) its central cross section. The object has the following parameters: $\mu_a = 0.02$ mm^{-1}, $\mu_s' = 1$ mm^{-1}, $g = 0.95$, and $2R = 10$ mm. The solid line shows a Gaussian approximation of the distribution cross section.

requires much computer time, which is inevitable even at the current stage of computer development.

In our simulations, we assumed that all the optical characteristics of the medium change in a jumpwise way on interfaces between different areas of an object being diagnosed. This assumption corresponds to a model where characteristic sizes of the regions of variation in any physical parameter considerably exceed the size of a spatially resolved pixel [30, 31]. We assumed that the reflection coefficient for all the interfaces is negligibly small. The probabilistic model of the
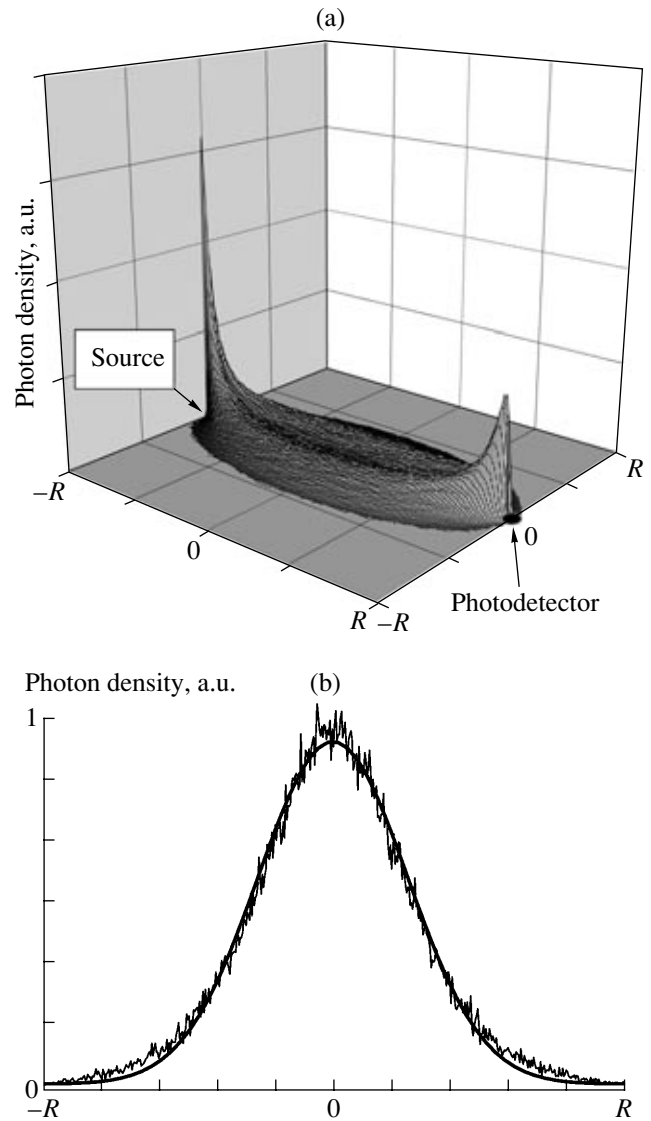
interaction of a photon with an element of a medium was introduced in a standard way [38]. The probability distribution of the mean free path lengths λ of a photon in a medium was described by the function

$$\rho(\lambda) = \mu_t^{-1} \exp(-\mu_t \lambda), \quad \text{where} \quad \mu_t = \mu_s' + \mu_a. \quad (2)$$

The scattering phase function $\rho(\mathbf{\Omega}, \mathbf{\Omega}')$ (with $\mathbf{\Omega}$ and $\mathbf{\Omega}'$ being the unit vectors along the wave vectors of the photon before and after scattering) was described by
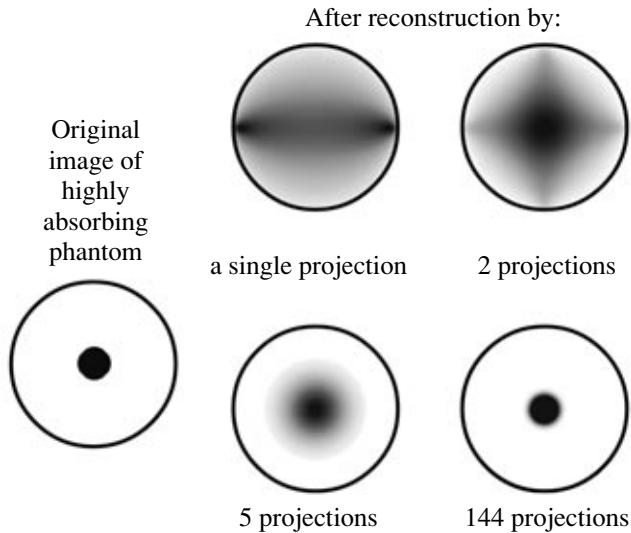
After reconstruction by:

Original image of highly absorbing phantom

a single projection   2 projections

5 projections   144 projections

Fig. 7. The spatial distribution $\Delta x \sim \Delta x_0 / \sqrt{N}$ depends on the projection width Δx_0 and the number of projections N employed for visualization. For $\Delta x_0 \approx R/2 = 35$ mm, we have $\Delta x \approx 3$ mm with $N = 144$. The situation is improved with $N = 1024$, when $\Delta x \approx 1.2$ mm.

the Henyey–Greenstein phase function [38, 43], which depends only on the scattering angle $\Theta = \arccos(\mathbf{\Omega} \cdot \mathbf{\Omega}')$,

$$\rho(\Theta) = f(\cos\Theta)/\|f\|, \tag{3}$$

$$f(x) = \frac{1 - g^2}{(1 + g^2 - 2gx)^{3/2}}. \tag{4}$$

Here, g is the mean cosine of the scattering angle. Within the optical range, the above-introduced parameters have the following characteristic values for the majority of biotissues: the transfer scattering coefficient is $\mu_s' = 1\text{–}10$ mm^{-1}, the absorption coefficient is $\mu_a = 0.005\text{–}0.05$ mm^{-1}, the anisotropy parameter is $g = 0.8\text{–}0.95$, and the mean free path length is $\lambda = 0.1\text{–}1$ mm [34, 35, 37].

In our numerical simulations, we calculated theoretical dependences of the distributions of photocount numbers for different positions of the photodetector (see Fig. 2). These dependences have confirmed that Eq. (1) provides a high accuracy in the approximation of the real experimental data. We have also determined the spatial distributions of the probability distribution for the propagation of detected photons through different points of a strongly scattering object both with (Fig. 5) and without (Fig. 6) strongly absorbing inclusions inside the scattering object. These simulations have demonstrated that, in the regime of multiple small-angle scattering, the cross-sectional views of probability distributions in the latter case can be approximated with Gaussian functions (Fig. 6b), which is apparently a consequence of the central limit theorem.
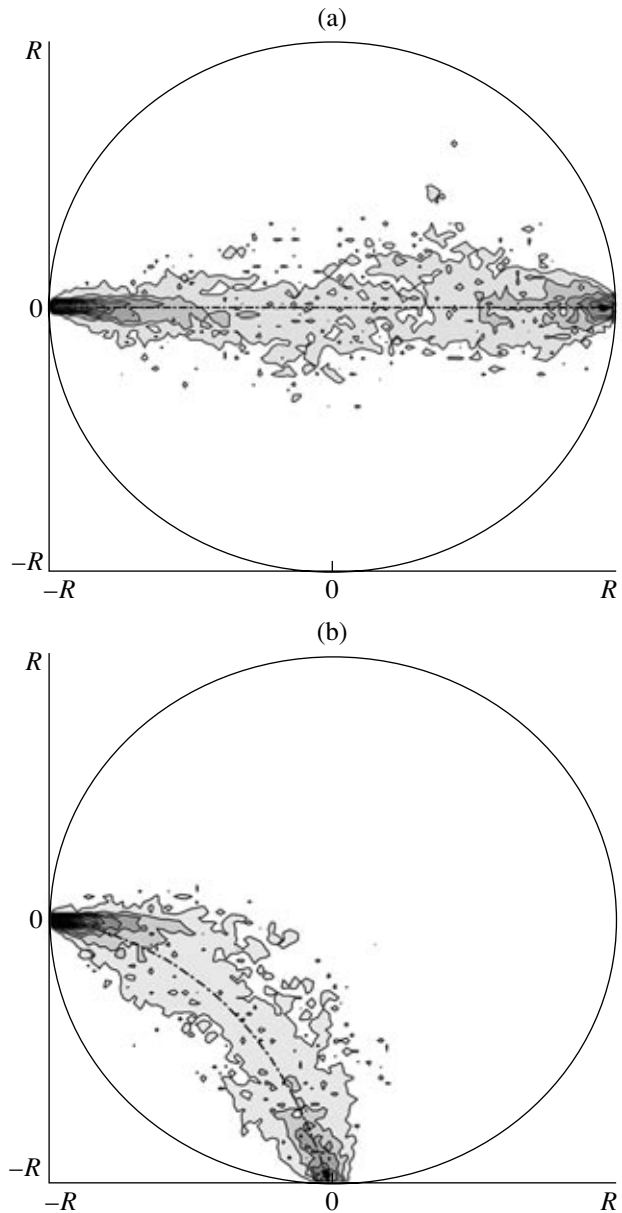

(a)

(b)

Fig. 8. Spatial distributions of the probability that photons pass through an object: (a) a light source and a detector are located on the opposite sides of the object ($\alpha = 0°$) and (b) transformation of the distribution for $\alpha = 90°$.

5. A FAST ALGORITHM FOR AN APPROXIMATE SOLUTION OF THE INVERSE PROBLEM

Conventional algorithms for an approximate solution of the inverse problem require the use of certain procedures in OT for the selection of a small part of the flux of detected photons. This requirement, in its turn, inevitably limits the maximum size of objects that can be diagnosed. Abandoning such a selection has brought us to the development of a new algorithm for an approximate solution of the inverse OT problem. This algorithm is described below in this section. The developed algorithm is statistical in its nature, and the infor-

mation concerning the internal structure of an object being diagnosed obtained through the use of this algorithm has a probabilistic character.

One of the most widespread algorithms for the solution of the inverse problem is the so-called projection algorithm [15, 16]. This algorithm has been efficiently used in X-ray tomography for a long time. One of the specific features of OT is that a flux of photons in this case propagates through a strongly scattering medium along complicated trajectories, which differ from straight lines. Due to the scattering, some part of this photon flux may pass through practically any point inside an object being diagnosed. Therefore, for any fixed position of a light source, this flux can be described with a three-dimensional (3D) function governing the probability distribution of photon propagation through different points inside an object. If we are now interested only in those photons that reach a detector, then we have to introduce 3D distributions for the conditional probability of the propagation of detected photons through different points inside the object corresponding to certain positions of the detector. These distributions of the conditional probability have finite widths (which may be quite large if no procedure for additional selection is applied) and can be calculated either analytically or by means of computer simulations. Our algorithm employs two matrices of input data. One of these matrices is quite real and corresponds to the case of an object with an inclusion. The second data matrix could be obtained in the absence of inclusions in the object (the reference matrix). When solving the inverse problem, we assume that, for any fixed position of the light source and the detector, the total probability to detect an inclusion inside an object is determined by the difference of the relevant elements of these two matrices. The distributions of the probabilities to detect an inclusion at different points of an object are set equal to initial distributions of the conditional probability (in the absence of inclusions) for the relevant fixed positions of the light source and the detector normalized to the corresponding total probability. Since all the distributions of the conditional probability obtained in this way (different pairs of matrix elements) are, in fact, different independent realizations of the same real situation, the distribution of the total probability to detect an inclusion at different points of an object can be described as a product of all the normalized distributions of the conditional probability. For an object with a complicated internal structure, this total probability distribution plays the role of a reconstructed image of the internal structure of the object.

Despite a comparatively large width of each of the 3D conditional probability distribution functions (which is on the order of half the distance between the light source and the detector if no selection procedure is applied), the resulting spatial resolution (the width of the total probability distribution) provided by this algorithm is quite good. The trick is that, by multiplying N^2
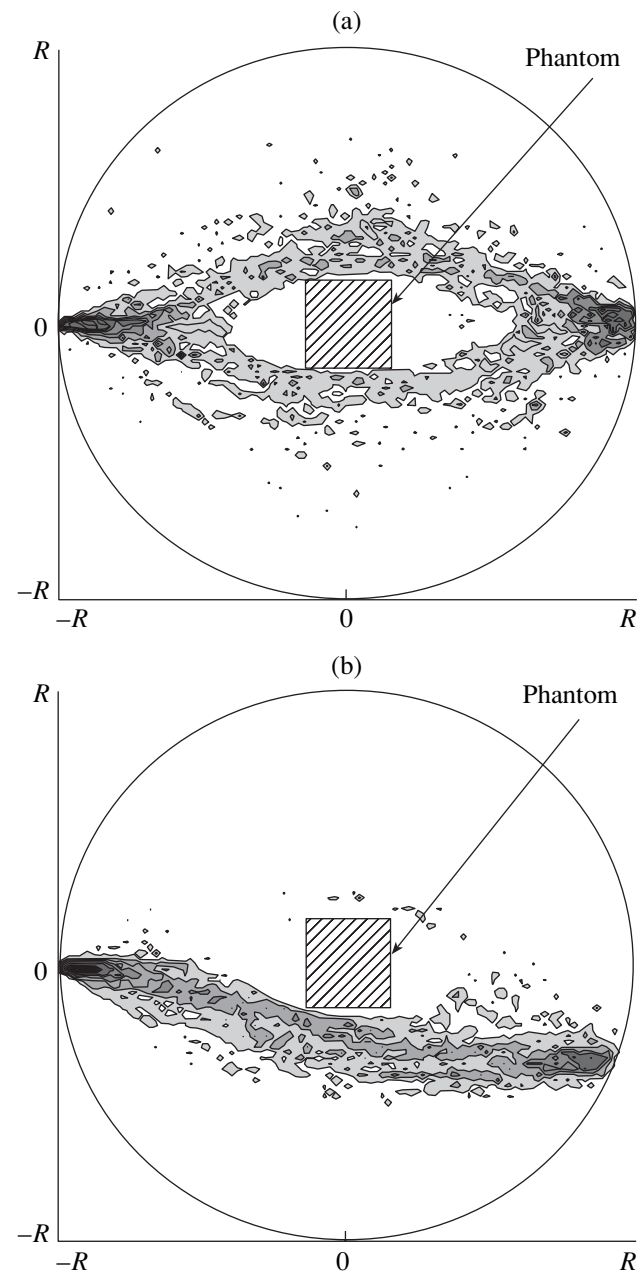

Fig. 9. Spatial distributions of the probability that photons pass through an object with an inclusion for different geometries of the arrangement of the light source and the detector (a, b). The object has the following parameters: $\mu_a = 0.02$ mm^{-1}, $\mu_s' = 1$ mm^{-1}, and $g = 0.95$. Parameters of the inclusion are $\mu_a = 2$ mm^{-1}, $\mu_s' = 1.4$ mm^{-1}, and $g = 0.95$.

(or N^4, see the discussion above) functions with nearly (because of the boundary conditions) Gaussian (in accordance with the central limit theorem) cross-sectional views (see Section 4), we reduce the resulting uncertainty in the spatial positions of inclusions by a factor of N (or N^2). This circumstance is sketched in Fig. 7.
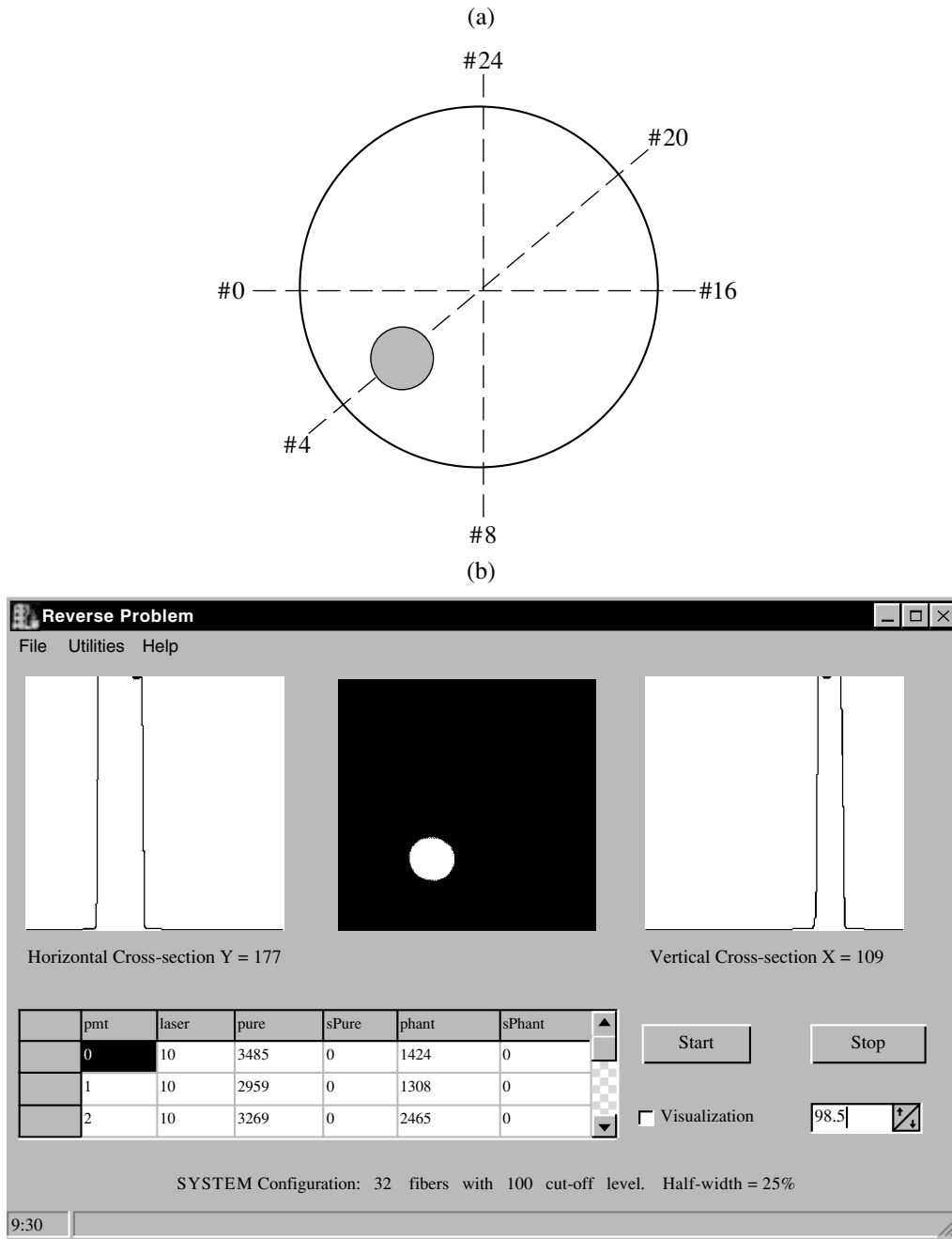
Fig. 10. (a) Experimental geometry and (b) the reconstructed image of a strongly absorbing inclusion as viewed on a computer screen. The central window displays a visualized inclusion image, while the right- and left-hand windows show the orthogonal cross sections of the distribution of the absorption coefficient. The object has the following parameters: $\mu_a = 0.05$ mm^{-1}, $\mu_s' = 1.4$ mm^{-1}, and $2R = 140$ mm. The strongly absorbing inclusion is characterized by $r = 12.5$ mm.

The implementation of the statistical algorithm described above requires an *a priori* information regarding the elements of the reference matrix and the initial 3D distributions of conditional probability (in the absence of inclusions) for different positions of the light source and the detector. To obtain such a data, we could, in principle, use the results of Monte Carlo simulation of the direct problem (see Section 4). However,

it is well known that the solution of such problems for 3D objects with linear sizes on the order of 300 and more scattering lengths is rather labor consuming. Specifically, simulation of a situation when the central detector registers 10^4 photons with an object diameter of 150 mm requires about 700–900 hours of computations. Therefore, calculating the 3D distributions of conditional probability required for the approximate
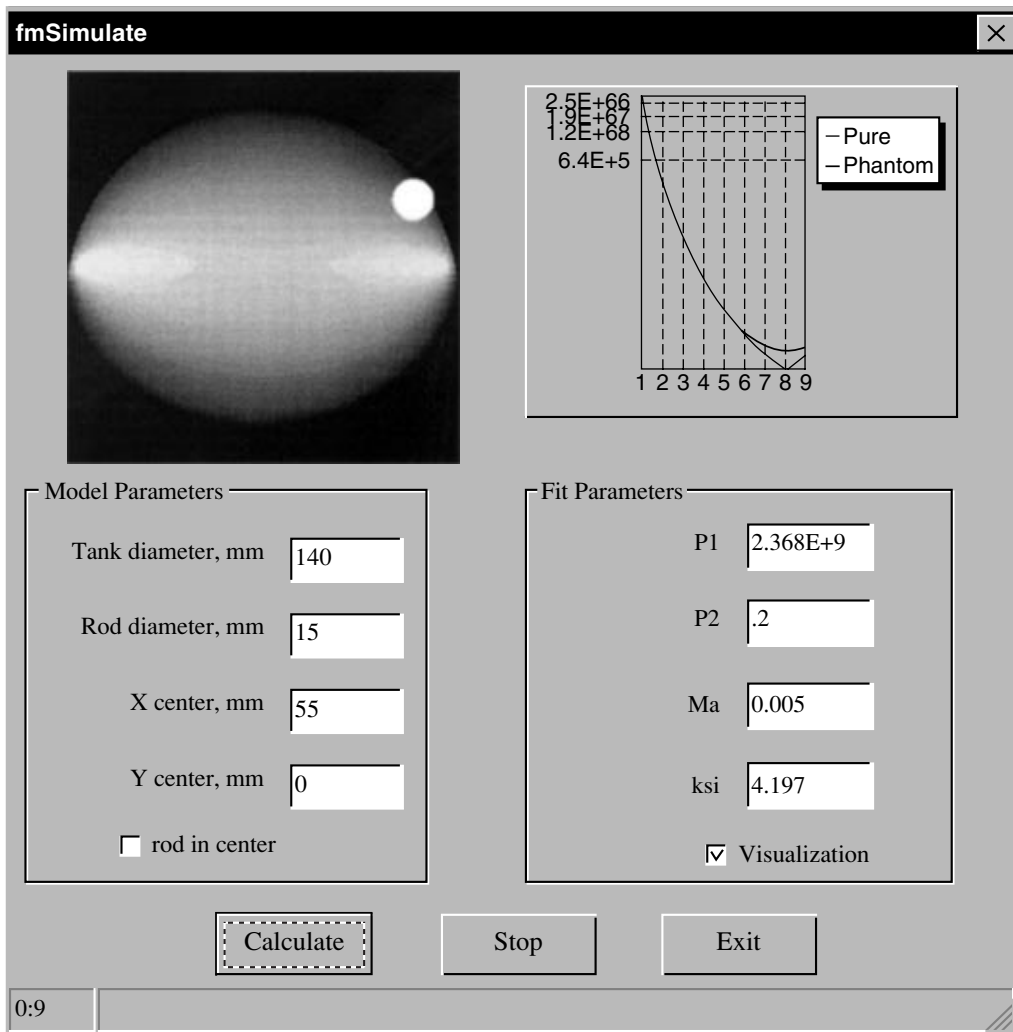
Fig. 11. Computer display view showing the fast solution of the direct problem. The upper left window demonstrates the geometry of the problem and the current transformation. The right-hand window displays the modeled dependence of the number of photocounts on the position of the light source and the detector. The object has the following parameters: $\mu_a = 0.005$ mm^{-1}, $\mu_s' = 1.4$ mm^{-1}, and $2R = 140$ mm. The strongly absorbing inclusion is characterized by $r = 7.5$ mm.

solution of the inverse problem, we employed only one such simulated (template) 3D distribution, which corresponded to a situation when the light source and the detector were placed on the opposite sides of an object being diagnosed. All the other distributions were calculated with the use of simple geometric transformations (scaling, see Section 3). We should also note that the scaling of conditional probability distributions inevitably gives rise to simulation errors, related to the deviations of the distributions thus calculated from the real distributions, which become distorted around the boundaries of an object [44]. This situation is illustrated by Fig. 8, which presents two distributions of this type simulated with the use of the Monte Carlo method. Distortions arising under these conditions are, in fact, reminiscent of geometric aberrations, which are well known in optics. Several well-developed algorithms can be employed to compensate for these aberrations.

The algorithm described above was implemented as a dedicated software, which allowed the computation time required to reconstruct an image of an inclusion from a 64^2 matrix with a PII-350 personal computer to be reduced to less than 5 min.

6. A FAST ALGORITHM FOR THE SOLUTION OF THE DIRECT PROBLEM

The possibility to scale conditional probability distributions allows a fast nonlinear algorithm for the approximate solution of the direct OT problem (calculation of the output data matrix by the method of cutting) to be developed for the case when a strongly absorbing inclusion is located inside a strongly scattering object. The same procedure of scaling conditional probability distributions in the absence of inclusions and some additional concepts can be employed for this
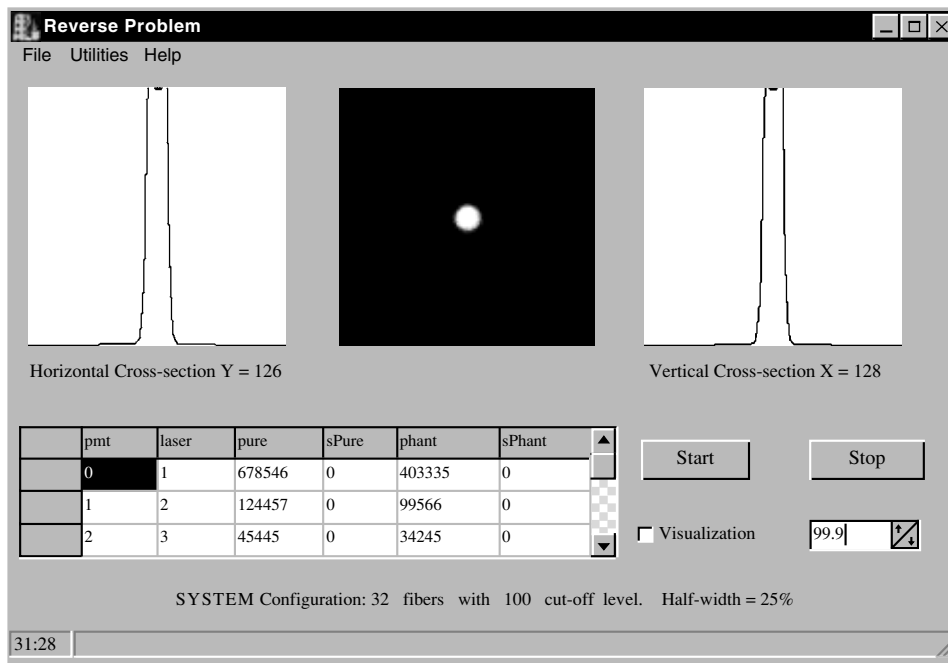
Fig. 12. Reconstructed image of a strongly absorbing inclusion. The object has the following parameters: $\mu_a = 0.005$ mm^{-1}, $\mu'_s = 1.4$ mm^{-1}, and $2R = 140$ mm. The inclusion is characterized by $r = 2.5$ mm.

purpose. The total probability that the detected photon passes through any cross section of the conditional probability distribution remains the same in the absence of inclusions for any fixed arrangement of the light source and the detector. When a strongly absorbing inclusion (with an absorption probability close to 1) arises inside an object being diagnosed, some part of the photons that could reach the detector pass through the absorbing inclusion, get absorbed, and never get detected. Therefore, a relatively small fraction of absorbed photons can be determined by simply cutting some part of the corresponding cross section of the conditional probability distribution (see Figs. 5b and 9). Specifically, for cylindrical inclusions, which were employed in our experiments, the width of the area of cutting was equal to the diameter of the cylinder.

The time required to solve the direct problem with the use of the algorithm described above with the only known distribution of the conditional probability that detected photons pass through an object being diagnosed in the absence of inclusions was equal to several minutes with allowance for the possibility to scale the known probability distribution (see the discussion above). The maximum deviation of the results obtained by this method from the real experimental data did not exceed 30–50%, which can be easily understood if we take into consideration possible reflection of light from the vessel walls and inclusions.

7. RECONSTRUCTION OF INCLUSION IMAGES

The input data for the developed software were obtained either in real experiments or by using the above-described algorithm for the simulation of the direct problem. In order to reduce the time of measurements, we studied the case of an axially symmetric arrangement of the inclusion in all the real experiments. Absorbing rods with diameters of 23, 15, or 10 mm were placed at the center of an object being diagnosed in these experiments, and only the position of the light source was changed during scanning. An N^2 overall matrix, which is necessary for the projection reconstruction algorithm, was obtained by translating the experimental data in the angle. To avoid systematic errors, which inevitably arise due to the translation of random errors, we preliminarily smoothed experimental dependences out before using them as the initial data for the reconstruction procedure. Figure 10 presents an image of an inclusion with a diameter of 15 mm reconstructed from the experimental data. The initial data for the reconstruction of images of inclusions shifted with respect to the center of an object and small-size inclusions were modeled with the use of the cutting method (Fig. 11). Figure 12 illustrates a reconstructed image of a strongly absorbing inclusion with a diameter of 5 mm. Figure 13 presents magnified reconstructed images of strongly absorbing inclusions with annular and square cross sections and a cylindrical strongly scattering inclusion. A characteristic halo is observed
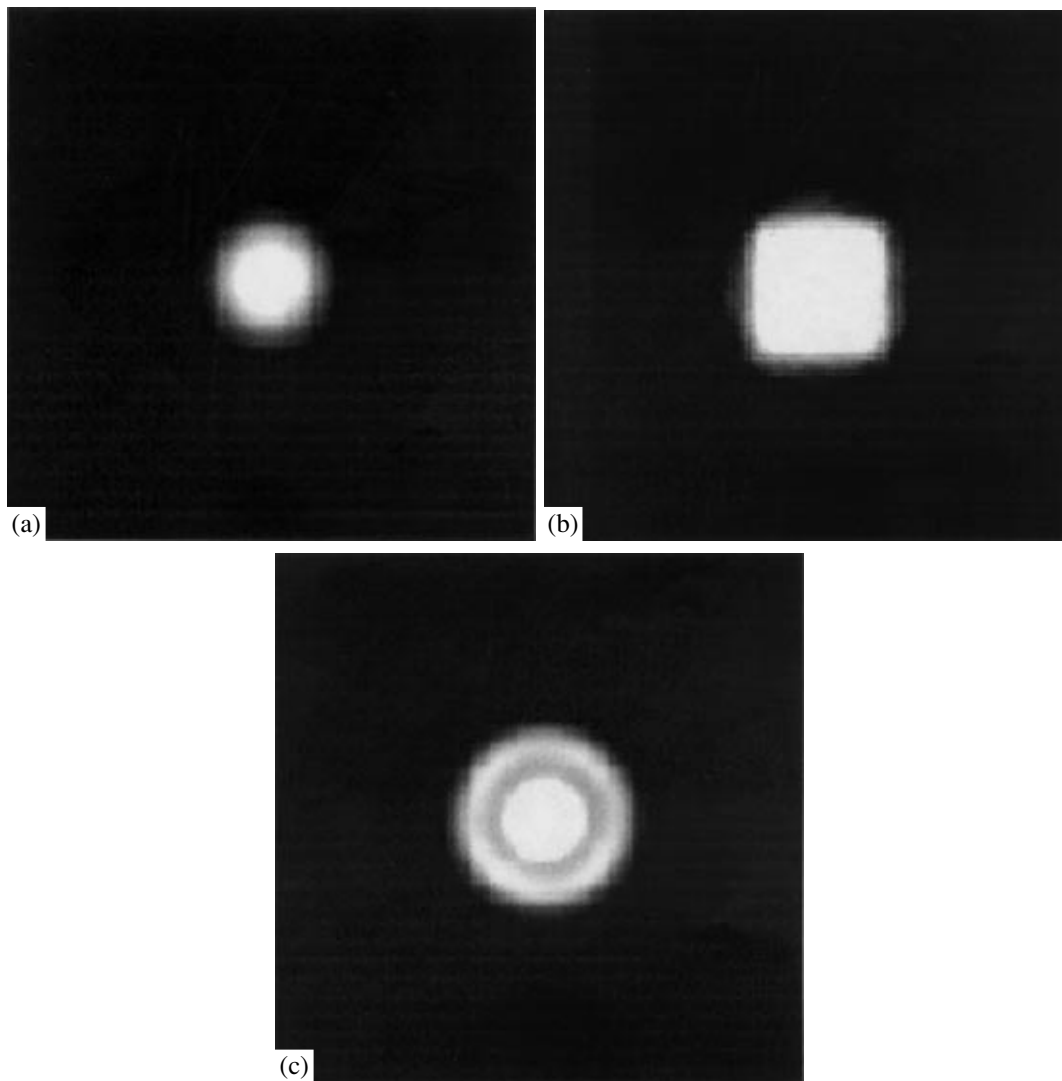
Fig. 13. Magnified reconstructed image of an inclusion in an object with a diameter of 140 mm with (a) a strongly absorbing cylinder with a diameter of 2 mm, (b) a similar parallelepiped with the size of the cross section equal to 4 mm, and (c) a strongly scattering cylinder with a diameter of 2 mm. A characteristic halo is observed around the reconstructed image in the latter case.

around the reconstructed image of the inclusion in the latter case. The appearance of this halo is due to the redistribution of the flux of detected photons because of scattering.

Our modeling has confirmed that the considered method does not impose any fundamental limitations on the spatial resolution. The less are the sizes of the inclusion to be reconstructed, the larger is the number of projections required for the solution of the inverse problem (the higher is the dimensionality of the input data matrix) and more time is required for the procedure of measurements (photon counting) at a single point (fixed positions of a light source and a detector) ensuring a reliable detection (above the noise level) of the inclusion shadow.

8. CONCLUSION

We have shown that abandoning conventional methods of selecting a certain part of the entire flux of detected photons in OT not only permits the size of an object being diagnosed to be considerably increased (up to 150 mm and more), but also allows the design of the OT system to be considerably simplified and the costs of such a system to be substantially reduced. Moreover, in view of the capabilities of the above-described approximate algorithm for the solution of the inverse problem, an acceptable spatial resolution can be achieved in this case (at least, for a certain class of tomographic problems).

The results of our preliminary experiments demonstrate that the minimum time of measurement (with a signal-to-noise ratio of $S/N \approx 1$) for the visualization of

a shadow of a strongly absorbing inclusion with a diameter of 5 mm located at the center of a strongly scattering (with the scattering coefficient $\mu_s = 1.4$ mm^{-1}) and weakly absorbing (with the absorption coefficient $\mu_a = 0.005$ mm^{-1}) object being diagnosed with a size of 140 mm is about 0.5 s in the case when the power of input radiation is 20 mW and a light source and a detector are located on the opposite sides of an object (the geometry that corresponds to a minimum output signal). Consequently, the total time required to measure all the elements of the 64×64 output data matrix never exceeds 30 min. The use of a multichannel photodetector (with 64 channels) would reduce the total time of measurements down to 0.5–1.0 min. In view of the capabilities of the above-described algorithm for the approximate solution of the inverse problem, it is exactly this time that is required for a tomographic reconstruction of the internal structure of an object being diagnosed.

At first glance, the necessity to use reference data, i.e., an *a priori* information on the detected photon fluxes in the absence of inclusions to be visualized for all possible positions of a light source and a detector, is a factor that limits the use of the algorithm described above. However, in certain situations (e.g., in a defectoscopy of standard articles), such data can be obtained both experimentally (through measurements performed on a template object in the absence of inclusions) and theoretically (by numerical simulation of the direct problem). In more complicated problems encountered, for example, in medical diagnostics, even not quite precise, statistically averaged reference data related to a certain typical object without specific features (inclusions) can be also employed. In particular, a reference matrix for the head of an "average" human can be used for a tomography of the head of some specific patient. The reconstructed image of the internal structure of an object obtained with the use of the above-described algorithm will have two characteristic spatial scales in this case. Smooth large-scale variations will be determined by deviations of certain parameters (e.g., the shape) of the head of a specific human from the head of an average human. Small-scale variations will be related to the presence of well-localized absorbing centers, e.g., hematomas. Due to the existence of two different spatial scales in the reconstructed image, not quite precise description of the reference data should not influence substantially the correctness of the solution of the inverse OT problem with the use of the above-described method.

REFERENCES

1. 1995, *Optical Tomography, Photon Migration, and Spectroscopy of Tissue and Model Media: Theory, Human Studies, and Instrumentation*, Chance, B. and Alfano, R.R., Eds. (SPIE), **2389**.

2. 1997, *Optical Tomography and Spectroscopy of Tissue: Theory, Instrumentation, Model, and Human Studies II*, Chance, B. and Alfano, R.R., Eds. (SPIE), **2979**.

3. 1999, *Optical Tomography and Spectroscopy of Tissue III*, Chance, B., Alfano, R.R., and Tromberg, B.J., Eds. (SPIE), **3597**.

4. 1997, *Developments in X-ray Tomography*, Bonse, U., Ed. (SPIE), **3149**.

5. 1986, *Structural Biological Applications of X-ray Absorption, Scattering, and Diffraction*, Bartunik, H.D. and Chance, B., Eds. (Orlando: Academic).

6. 1993, *MRI in Practice*, Westbrook, C. and Kaut, C., Eds. (Oxford: Blackwell).

7. 1991, *3D Imaging in Medicine*, Udupa, J.K. and Herman, G.T., Eds. (Boca Raton: CRC).

8. Sarvazyan, A.P., 1983, *Biophysical Foundations of Ultrasonic Medical Diagnostic*, (Gor'kii), p. 80.

9. 1996, *Photon Propagation in Tissues*, Chance, B., Delpy, D.T., and Muller, G.J., Eds. (SPIE), **2626**.

10. 1996, *Proceedings of Photon Propagation in Tissues II*, Benaron, D.A., Chance, B., and Muller, G.J., Eds. (SPIE), **2925**.

11. 1998, *Proceedings of Photon Propagation in Tissues III*, Benaron, D.A., Chance, B., and Ferrari, M., Eds. (SPIE), **3194**.

12. 1989, *Photon Migration in Tissues*, Chance, B., Ed. (New York: Plenum Press).

13. Ho, P.P., Wang, L., Liang, X., *et al.*, *Opt. Photonics News*, **4**, 23.

14. Feng, S.C., Zeng, F.-A., and Chance, B., 1993, *Proc. SPIE*, **1888**, 78.

15. Herman, G.T., 1980, *Image Reconstruction from Projections: The Fundamentals of Computerized Tomography* (San Francisco: Academic Press).

16. 1987, *Basic Methods of Tomography and Inverse Problems: A Set of Lectures*, Sabatier, P.C., Ed. (Bristol: Hilger A.).

17. Wang, L., Ho, P.P., Liu, C., *et al.*, 1991, *Science*, **253**, 769.

18. Proskurin, S.G., Yamada, Y., and Takahashi, Y., 1995, *Proc. SPIE*, **2389**, 157.

19. Wells, K., Hebden, J.C., Schmidt, F.E., and Delpy, D.T., 1997, *Proc. SPIE*, **2979**, 599.

20. Hee, M.R., Puliafito, C.A., Schuman, J.S., and Fujimoto, J.G., 1996, *Optical Coherence Tomography of Ocular Diseases* (Thorofare: SLACK Inc.).

21. 1996, *CIS Selected Papers: Coherence-Domain Methods in Biomedical Optics*, Tuchin, V.V., Ed. (SPIE), **2732**.

22. Tearney, G.J., Brezinski, M.E., Hee, M.R., *et al.*, 1995, *Proc. SPIE*, **2389**, 29.

23. 2000, *Coherent Domain Optical Methods in Biomedical Science and Clinical Applications IV*, Tuchin, V.V., Izatt, J.A., and Fujimoto, J.G., Eds. (SPIE), **3915**.

24. O'Leary, M.A., Boas, D.A., Chance, B., and Yodh, A.G., 1995, *Opt. Lett.*, **20**, 426.

25. Papaioannou, D.G., Colak, S.B., and Hooft, G.W., 1995, *Proc. SPIE*, **2626**, 218.

26. Bocher, T., Beuthan, J., Minet, O., *et al.*, 1995, *Proc. SPIE*, **2626**, 283.

27. Sevick-Muraca, E.M., Burch, C.L., Frisoli, J.K., *et al.*, 1993, *SPIE Institutes for Advanced Optical Technologies*, **IS 11**, 485.

28. 1993, *Photon Migration and Imaging in Random Media Tissues*, Chance, B. and Alfano, R.R., Eds. (SPIE), **1888**.

29. 1994, *Selected Papers on Tissue Optics: Applications in Medical Diagnostics and Therapy*, Tuchin, V.V., Ed. (SPIE), **MS102**.

30. 1993, *Medical Optical Tomography: Functional Imaging and Monitoring*, Muller, G., Chance, B., Alfano, R., *et al.*, Eds. (SPIE), **IS11**.

31. 1998, *Selected Papers on Optical Tomography: Fundamentals and Applications in Medicine*, Minet, O., Mueller, G.J., and Beuthan, J., Eds. (SPIE), **MS147**.

32. Proskurin, S.G., Takahashi, S., Kwee, I.W., *et al.*, 1997, *Proc. SPIE*, **2979**, 261.

33. Chursin, D.A., Shuvalov, V.V., and Shutov, I.V., 1999, *Quantum Electron.*, **29**, 921.

34. 1994, *Cell and Biotissue Optics: Applications in Laser Diagnostics and Therapy*, Tuchin, V.V., Ed. (SPIE), **2100**.

35. 1993, *Optical Methods of Biomedical Diagnostics and Therapy*, Tuchin, V.V., Ed. (SPIE), **1981**.

36. Pan, Y. and Farkas, D.L., 1998, *J. Biomed. Opt.*, **3**, 446.

37. Roggan, A., Friebel, M., Dorschel, K., *et al.*, 1999, *J. Biomed. Opt.*, **4**, 36.

38. 1978, *Wave Propagation and Scattering in Random Media*, Ishimaru, A., Ed. (New York: Academic), **1** and **2**.

39. Arridge, S.R., Schweiger, M., Hiraoka, M., and Delpy, D.T., 1993, *Med. Phys.*, **20**, 299.

40. Gantmacher, F.R., 1959, *The Theory of Matrices* (New York: Chelsea).

41. Gerrard, A. and Burch, J.M., 1975, *Introduction to Matrix Methods in Optics* (New York: Wiley).

42. Goertz, G. and Kalos, M.H., 1958, *Monte Carlo in Transport Problems* (London: Pergamon).

43. 1970, *Principles of Optics*, Born, M. and Wolf, E., Eds., 2nd ed. (Oxford: Pergamon).

44. Volkonskii, V.B., Kravtsenyuk, O.V., Lyubimov, V.V., and Skotnikov, V.A., 1999, *Opt. Spectrosc.*, **87**, 422.

45. 1989, *Technical Means of Medical Introscopy*, Leonov, B.I., Ed. (Moscow: Meditsina).

46. Tkachun, R.N., 1994, *Kardiologiia*, **34**, 69.